Downlink Multi-user sub-THz Communication with a Programmable Metasurface

Fahid Hassan*, Zhambyl Shaikhanov†, Jeffrey Lei‡, Hichem Guerboukha§,Hou-Tong Chen¶,Chun-Chieh Chang¶, Sadhvikas Addamane ‖, Michael P. Lilly ‖, Daniel M. Mittleman‡, and Edward W. Knightly*
*Department of Electrical and Computer Engineering, Rice University
†Department of Electrical and Computer Engineering, University of Maryland
‡School of Engineering, Brown University
§Electrical and Computer Engineering Department, University of Missouri–Kansas City
¶Center for Integrated Nanotechnologies, Los Alamos National Laboratory
‖Center for Integrated Nanotechnologies, Sandia National Laboratories

***Abstract*—Among the many challenges in realizing wireless networks above 100 GHz, multi-user access remains one of the least explored. Traditionally, multi-user multiplexing at lower frequencies requires the implementation of one RF chain per data stream (user). Adapting such technology to higher frequencies above 100 GHz incurs prohibitively complex design and fabrication challenges, especially when scaling to many users. Here, we propose a fundamentally new approach that enables sub-terahertz multi-user access without any RF chains. Our design consists of a programmable, transmissive metasurface and a single monochromatic sub-terahertz source. We use the metasurface to modulate the phase and amplitude of the transmitted sub-THz wave using random voltage patterns, producing a high-entropy wavefront that has unique angular-dependent patterns. Generating these spatially diverse responses enables concurrent transmission of distinct information symbols to multiple users at different angular locations. We demonstrate the feasibility of this approach using both numerical simulations and experimental studies, showcasing the ability to serve multiple users simultaneously with distinctive data streams, even in scenarios with minimal angular separation between users. The study paves the way for a new architecture for sub-THz spatial multiplexing with no RF chains.**

***Index Terms*—Terahertz, Multi-User WLANs, Metasurfaces**

I. Introduction

With the rapid growth in demand for wireless capacity, multi-user (MU) multiplexing will be a key tool for scaling data rates to terabits per second (Tb/sec) [1]–[3]. MU multiplexing enables simultaneous transmission of multiple independent data streams towards multiple receivers (Rxs) within the same broadcast sector, thereby increasing spectral efficiency and network capacity. In fact, the technique has been widely adopted in wireless standards at lower frequencies, such as IEEE 802.11ay operating at 60 GHz [4] and IEEE 802.11be (Wi-Fi 7) operating below 6 GHz [5]. Prior designs based on these standards typically employ large antenna arrays driven by radio frequency (RF) chains, where the modulation of the signal happens at baseband and then one RF chain per data stream [6]–[8] is needed to up-convert the signal to RF. The number of simultaneously transmitted data streams is thus limited by the available number of RF chains at the transmitter (Tx).

In principle, MU multiplexing is particularly well suited for millimeter-wave and sub-THz frequencies, where highly directional beams will be mandatory to overcome high free-space path loss [9]–[11]. These pencil-like beams can permit spatial multiplexing among users of the same frequency band without interference. Unfortunately, incrementally improving today's MU network designs to scale to the sub-THz regime has not proved fruitful. This is because at such high frequencies, the fabrication of arrays with a large number of RF chains (and their constituent components such as frequency multipliers, filters, and mixers) is notoriously challenging due to the high power consumption, development complexity, and prohibitive cost associated with current designs [12]–[15]. Recent efforts have aimed to reduce the required number of RF chains by employing methods such as array-of-subarrays grouping [16], [17], hierarchical modulation [18], and non-orthogonal multiple access [19]–[21]. Although these approaches reduce the complexity of MU multiplexing, the number of served users still correlates with the number of RF chains at the Tx side.

In this paper, we demonstrate a new approach to sub-THz downlink MU multiplexing, which *requires no RF chains and no antenna arrays*. Our approach employs a switchable metasurface that reconfigures at the symbol rate to transform a monochromatic sub-THz input into a a high-entropy wavefront that results in angularly varying amplitude and phase responses. This angular response allows to send multiple independent directional data streams to multiple users simultaneously. The metasurface consists of many electrically reconfigurable pixels, each controlled by an analog voltage. As this is an analog signal, there are an extremely large number of possible metasurface configurations (the number of possible values for the control voltage raised to the number of pixels) which are switched at the symbol rate. The key realization,

FH, ZS, and EWK's research was supported by Cisco and Intel, by NSF grants 2402783, 2211618, 2148132, and 1955075, and by ARO DURIP grant W911NF-23-1-0340. JL and DMM research was supported by NSF grants 1954780, 2211616, and 2433924, and by Air Force Office of Scientific Research grant FA9550-221-0412. This work was performed, in part, at the Center for Integrated Nanotechnologies, an Office of Science User Facility operated for the U.S. Department of Energy (DOE) Office of Science by Los Alamos National Laboratory (Contract 89233218CNA000001) and Sandia National Laboratories (Contract DE-NA-0003525).

illustrated in Fig. 1, is that, for any given set of analog control voltages $\{V_i\}_{i=1,\ldots,p}$ (one for each of the p column-shaped pixels) applied to the metasurface, an incident single-frequency plane wave interacting with the entire metasurface produces a far-field scattered wave with a unique (and possibly very complicated) amplitude and phase profile $E(\theta, \phi)$. As a result, users at different angular locations may simultaneously receive signals with different in-phase and quadrature (I and Q) values. Thus, the metasurface can effectively modulate the THz wave's phase and amplitude such that a single metasurface configuration can concurrently transmit distinct information symbols to users positioned at different angular locations. We refer to this idea as *angular-dependent MU symbols*. The set of analog control voltages $\{V_i\}$ can then be switched at the symbol rate, simultaneously serving multiple users with unique data streams.

In particular, we make the following three contributions. First, we introduce the idea of Angular-dependent symbols using a simple model that qualitatively mimics the result of illuminating the metasurface. We show how a randomly excited metasurface can produce high-entropy wavefront that results in angularly varying amplitude and phase responses. This allows us to send different information symbols for users located in different directions from the metasurface. In addition, we show how selecting different random voltage patterns can result in different symbols received in each user's direction, allowing for more symbol options for each user's angle. Next, we discuss how the Tx can utilize such angular-dependent symbols to facilitate MU transmission to users in different directions by selecting a specific subset of metasurface configurations that result in the user's desired symbol combinations based on the user's numbers, modulation rates, and locations.

Second, we present an experimental realization of our system, employing a programmable, transmissive metasurface featuring an array of metallic square-shaped split-ring resonators (S-SRR). The S-SRRs are grouped into 16 column-shaped pixels, each with its control voltage pad. Under different voltage biases, the S-SRR can produce different amplitude modulations and phase shifts to the transmitted electromagnetic (EM) wave. Thus, we can electrically control the response of the metasurface by dynamically changing the voltage bias applied to the array of S-SRRs. Next, to generate a diverse set of configurations with angular-dependent responses, we experimentally pre-characterize the metasurface response at numerous angles (relative to the broadside direction) under numerous random non-uniform control voltage configurations. i.e., by applying different voltage biases to different S-SRRs across the metasurface. We show how generating a large set of such configurations results in a diverse set of constellation points from which the Tx can choose. Next, we show how subsets of configurations can be selected to correspond to directional symbols that enable different data streams to be transmitted simultaneously to multiple Rxs for selected modulation rates.

Finally, we conduct over-the-air measurements using a high-resolution THz time-domain-spectroscopy (TDS) system to evaluate our system's performance. Specifically, we generate a set of 1000 random configurations and evaluate the available symbol options achievable at two example Rx angles $\theta_1 = 50^\circ$ and $\theta_2 = 15^\circ$ from the metasurface broadside. Next we assess the achievable single-user (SU) time shared and MU rates achieved for the two users under different signal-to-noise ratios (SNRs). Our results show that in moderate SNR scenarios with sufficient angular separation, maximal MU gains of twofold are achievable when two users are served simultaneously. In addition, we study the relation between the two users' angular separation and the achievable network MU rate. Our results show that significant MU Gain is attainable even if the two users have angular separation as slight as 2°, while the maximum gain of twofold is achievable with only 10° angular separation.

The rest of our paper is organized as follows: In Section II, we summarize the related work and discuss the significance of our work compared to the literature. Section III and Section IV introduce the key concept of angular-dependent symbols and how it is utilized to achieve MU multiplexing. Section V discusses our experimental setup and the experimental evaluation. And Section VI concludes the paper.

II. Related work

mmWave to THz MU theoretical work. As sub-THz communications is a rapidly growing research area, many works have studied its different aspects, including MU multiplexing. This research encompasses a range of approaches, including intelligent reflective surfaces (IRS) based MU communication [22]–[24], orbital angular momentum (OAM) based MU multiplexing [25], and more conventionally, phased array based MU multiplexing [26]–[28]. While providing essential evaluations to understand different aspects of MU multiplexing for THz links, the aforementioned papers do not provide an implementation or experimental demonstration of the proposed schemes. In contrast, we implement and provide an experimental evaluation and demonstration of our system and discuss the potential and limitations to enable further understanding of the proposed system.

Experimental demonstration of MU multiplexing above 100 GHz. Experimental evaluation for sub-THz MU methods using THz angularly dispersive links with leaky wave antennas was introduced in [29]. While this work introduces new techniques to create spatially orthogonal channels, the data streams are still generated at baseband and then upconverted using RF components. On the other hand, our system offloads data generation to the metasurface, leading to reduced hardware cost and power consumption associated with RF components. Thus, enabling both MU spatial multiplexing and data generation with a simplified Tx architecture.

RF chain-free MU communication below 10 GHz. There have been few works in the literature that explored RF chain-free MU communications at lower frequencies. For instance, works in the sub-6 GHz range include direct antenna modulation solution [30] and a 2x2 metasurface-based MIMO

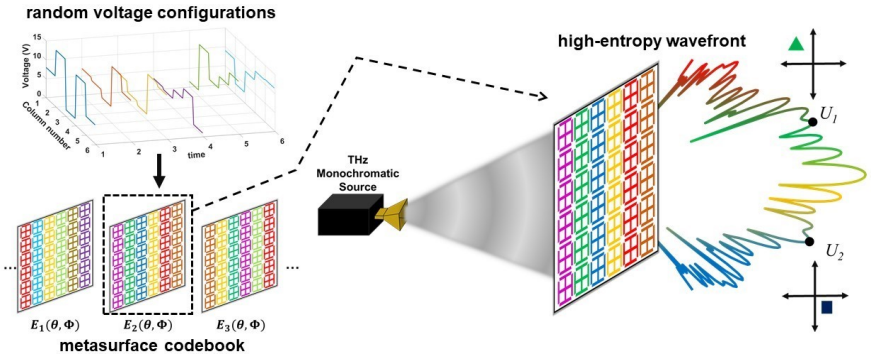

Fig. 1: A schematic of the metasurface-based MU transmission scheme.

system [31]. In addition, frequency harmonics multiplexing using space-time metasurfaces has been introduced in [32], and a metasurface based MU on-off keying (OOK) Tx at 10 GHz was introduced in [33]. While these works explore the idea of eliminating the need for RF chains at lower frequencies, our system is the first demonstration of this capability in the sub-THz range. Our Tx architecture utilizes a sub-THz metasurface that can scatter the signal with different phase and amplitude into different direction, offering a new approach to exploit sub-THz spectrum without any need for the complex electronic front ends that are generally considered to be one of the key limiting factors in implementing networking at these frequencies.

III. Angular-Dependent MU Symbols

First, we illustrate the idea using a simplified model that qualitatively mimics the result of illuminating our metasurface with a narrowband plane wave, thus producing a scattered wave in transmission, as in Fig. 1. According to the Huygens-Fresnel principle, the total response of the metasurface at any Rx's location is the linear superposition of the diverging spherical waves scattered from each of the excited metasurface's pixels, weighted by the distance between the pixel and the user. This can be mathematically approximated as [34]:

$$E(x,y,z) = \frac{e^{jkz}}{j\lambda z}\iint E(x',y',0)\; e^{\frac{jk}{2z}[(x-x')^2+(y-y')^2]}dx'dy' = E_M(x,y,z)\; e^{j\phi_M(x,y,z)}, \tag{1}$$

where $E(x',y',z'=0)$ is the complex profile of the metasurface, i.e., it is the phase and amplitude of the spherical wave of the emitter at location $(x',y',z=0)$ causes to the incident plane wave. Moreover, λ is the wavelength, $k=\frac{2\pi}{\lambda}$ is the wave number. Thus, we can write $E_M(x,y,z)$ and $\phi_M(x,y,z)$ as the total amplitude and phase response due to the metasurface at location (x,y,z), respectively.

In our model, the metasurface's profile is considered a linear array of 16-point emitters (corresponding to the real device's p = 16 adjacent column-shaped pixels, described further below). As in our experiments, these emitters are spaced by $\frac{5}{8}\lambda$ and emitting spherical waves at 147 GHz ($\lambda = 2.04$ mm). The amplitude and phase of each of the 16 spherical wave can be adjusted in the model to have any value within the range accessed by the metasurface used in our experiments. Specifically, the phase and amplitude of the emitters are chosen from a range of phase shifts of $0^\circ - 37^\circ$ and an amplitude modulation range from 1 to 0.5, respectively. These ranges are experimentally determined by normal-incidence transmission measurements as a function of the control voltage applied to the metasurface.

Fig. 2 shows the computed information symbols (presented in I-Q space) observed by different users, i.e., at various angular locations θ from the metasurface broadside, with three exemplary randomly generated amplitude and phase configurations (corresponding to three different sets of voltages $\{V_i\}$ applied to the metasurface). Note that here, we are using polar coordinates to describe the Rxs' locations relative to the metasurface; the angular location of a Rx can be described by an angle θ, where $\theta = \tan^{-1}\left(\frac{x}{z}\right)$, as we assume for simplicity that all Rxs have the same y coordinate.

We can see from Fig. 2 that for a given configuration, the constellation points shift significantly with changes in the users' angular location, occupying the entire 2π range. We emphasize that this 2π coverage in I-Q space is achieved even though the metasurface's phase modulation range is only about 37°. This is due to the effect of scattering from an essentially random surface. This indicates that, with a single set of control voltages, the 16-pixel metasurface can send different I-Q points to users at different locations. Moreover, for a particular user location θ, a change in the voltage configuration produces a marked shift in the constellation point for that user. Since there are a very large number of possible voltage configurations (only 3 of which are illustrated in Fig. 2), we can realize configurations for many sets of distinct I-Q points for a given collection of Rx locations.

By exploring the many possible control voltage configurations $\{V_i\}$, we can generate a rich set of constellation options for simultaneously serving multiple users. We specifically choose particular configurations that exhibit the necessary properties (phase and amplitude of the scattered wave) to transmit all symbol options to users positioned at different angular locations based on their supported modulation rates

(bits/symbol). A codebook of such configurations would be required to accommodate multiple user access scenarios (varying combinations of users, their locations, and modulation rates).

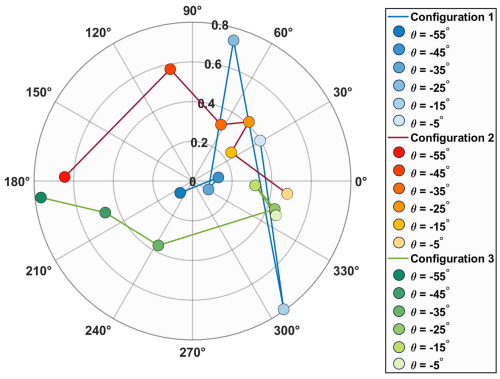

Fig. 2: MU constellations corresponded to 3 different randomly generated configurations.

IV. MU Transmission with Angular-Dependent MU Symbols

Our objective is to provide a codebook consisting of subsets of configurations that enable the Tx to send independent, well-separated symbols to users in different directions. Our solution has two components. First, we generate an angular I-Q space by generating a large number of random metasurface configurations. The random configurations provide diverse angular-specific symbol options from which the Tx can choose. Second, we sub-select a number of these configurations with the necessary properties that can achieve independent streams for the users corresponding to their modulation rates.

In particular, in the first component, we configure a large number of randomly generated configurations to characterize the achievable angular I-Q space. To realize each of these configurations, we spatially program the metasurface columns with randomly selected voltage biases. Specifically, for each column, we apply a different voltage bias chosen uniformly at random from the range of available voltage biases. As a result, each channel introduces a random amplitude and phase shift into the transmitted THz wave. Consequently, as the signal received at different angular directions comprises the superposition of signals scattered from all channels, different users at different angular directions receive a different version of the information symbol.

In the second component, the Tx is tasked with programming the metasurface at each symbol epoch to a new pre-characterized configuration such that Rx i located at angle θ_i receives its correct data symbol. In general, N users with modulation rates M_i, require $2^{(\sum_{i=1}^{N} M_i)}$ symbol combinations so that the users can have independent data streams. In order to minimize the symbol error rate at the Rx, the transmitted symbols would ideally be uniformly spaced over the I-Q space as in standard QAM constellations. Unfortunately, however, a realistic metasurface might not be able to precisely achieve all the required phase and amplitude modulations. Therefore, our objective is to find configurations for all possible symbol combinations for each user that yield sufficient separation for a Bit Error Rate (BER) requirement. Therefore, to design the codebook, we first generate a large set O of angularly dependent configurations, where $|O| \gg 2^{(\sum_{i=1}^{N} M_i)}$. Each configuration results in the transmission of a unique set of symbols at different angles. Next, from the generated responses, we find a subset of configurations that jointly maximize the separation between the symbols in each user's I-Q space.

For instance, Fig. 3 illustrates an example of a subset. Here two users (U_1 and U_2) are simultaneously served with modulation rates $M_1 = M_2 = 2$ (bits/symbol). The Tx finds $2^{2+2} = 16$ configurations that result in all possible symbol combinations the two users might request. For example, configurations 1-4 (shown with red circles) result in one symbol option for user U_1 while the same configurations result in 4 different symbols for U_2.

Thus, the pre-designed codebook consists of multiple subsets of configurations, each optimized for a different combination of users, locations, and respective modulation rates. Since the Rx's SNR constrains the modulation rate, the Tx chooses the relevant subset from the pre-designed codebook upon knowing the users' locations and SNRs.

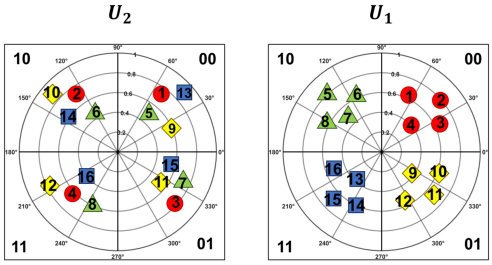

Fig. 3: Example of 16 configurations used to transmit simultaneous, independent symbols with modulation rates of 2 bits/symbol to two different users.

V. Experimental Evaluation

In this section, we first introduce the metasurface device and the experimental setup we use to conduct our measurements. Next we discuss our over-the-air experiments and evaluate the key properties of our system.

A. Experimental Setup

In our design, the metasurface comprises $p = 16$ columns (channels), each 1.26 mm wide, each consisting of 6×155 individual S-SRRs. Within each column, all of the SRRs are electrically connected to a single pad for external control of the applied bias, as can be seen in Fig. 4. All 16 columns share a common ground, a separated pad which has an ohmic connection to the doped epilayer. For programming the metasurface into various configurations, we employ a National Instruments DAC card (NI PCIe-6738) with a 16-bit output

voltage resolution. We randomly assign a voltage bias to each column to create a single random metasurface configuration.

To measure the response (phase and amplitude) generated from each of these configuration, we utilize a commercial THz time-domain system [35], which generates a picosecond time-domain THz pulse that is transmitted and received by two fiber-coupled sensor heads acting as a Tx and a Rx as shown in Fig. 4. The transmission power of the system is approximately 10 μW spread across the entire spectrum range from 100 GHz to around 2 THz. Due to such low transmit power, the effective range is limited, and we adjust the distances in our experimental test bed accordingly.

In our measurements, the metasurface is fixed at a distance of 8 cm from the Tx, with the metasurface and the Tx's antenna aligned to ensure the transmitted beam has a normal incidence on the metasurface. The Rx is placed at a fixed distance of 45 cm in the line of sight of the metasurface and is mounted on a rotation stage, allowing free rotation to permit measurements at various angular directions. To characterize the metasurface's response, we rotate the Rx antenna and collect the time domain signal at each of the Rx's intended angles for each configuration. Then, we extract the phase and amplitude of the targeted frequency of 147 GHz by Fourier transform.

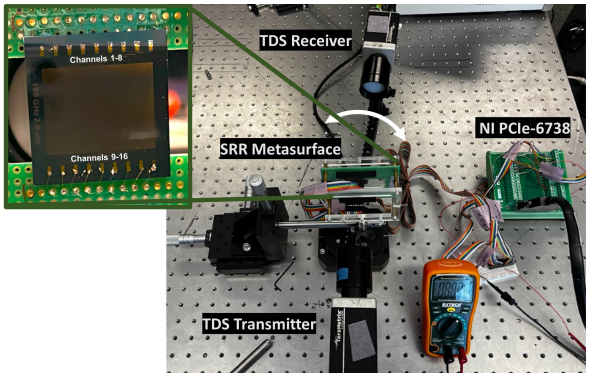

Fig. 4: Our experimental setup.

We note that THz metasurface technology is currently an active area of research. The metasurface used in our measurements exhibits a relatively low switching speed due to the RC time constant of the structure. Thus, although our results demonstrate the feasibility of the approach for MU networking, a faster metasurface would be required for compatibility with envisioned high-speed applications. We note that several groups have recently developed metasurfaces with switching speeds in the GHz range [36]–[38], so there is a clear route to implementation at high data rates.

B. Characterizing the Square-shaped SRR THz metasurface

Figure 5a shows a schematic of S-SRR. The array of S-SRR is fabricated via photolithography on a 1.5-μm-thick n-doped GaAs epilayer atop a semi-insulating GaAs substrate similar to the one introduced in [39], [40]. The metallization which forms the SRRs establishes a Schottky contact to the underlying semiconductor, such that an applied reverse bias can dynamically modify the resistivity of the underlying depletion zone. This manipulation of carrier density in the depletion zone effectively changes the loss of the gap in the split ring, thereby modulating the transmission amplitude and phase of free-space terahertz radiation at frequencies near the SRR resonance [39], [40]. The degree of amplitude and phase response depends on the magnitude of the applied bias, with a roughly linear variation up to a point, followed by saturation due to carrier depletion.

We experimentally characterize the response of the S-SRR by applying a range of reverse bias values from 0 to 18 V with a resolution of 0.1 V. We illuminate the device with a broadband THz beam at normal incidence and measure the transmitted signal as a function of bias voltage. Figure 5b shows the amplitude modulation and phase shift for the tested range of reverse voltage biases for our device. Here, The amplitude modulation is defined as the amplitude transmission at a given bias divided by the transmission amplitude at 0 V bias. i.e., $t(v)/t(v=0)$. Similarly, the phase shift is defined as the difference between the phase of the signal with 0 V and the phase of the signal when a bias V is applied. i.e., $\phi(v=0)-\phi(v)$. We see from the figure that increasing the voltage bias increases the transmission amplitude, as expected. We observe a dynamic range of (0.5 -1). In addition, a dynamic phase shift range of approximately 50° is achievable. We observe that at higher voltage levels, saturation occurs as the Schottky barrier becomes fully depleted of free charges. Consequently, we restrict our voltage bias range, used for generating random voltage configurations, from 0 to 15 V, as no significant alterations in both phase and amplitude are noted beyond 15 V. Furthermore, we opt for a resolution of 0.25 V, aligning with the level at which we observe a reliably repeatable change in phase. With this range and resolution, we can access 61 unique voltage values, which can be applied to each SRR, allowing a huge number of different random configurations the Tx can use to generate different angular-dependent symbols. For instance, for our 16 columns metasurface, with independent control of each column, we have a total of $61^{16} \approx 3.7 \times 10^{28}$ different configurations the Tx can generate. Obviously, not all of these possibilities are independent or sufficiently distinct from each other; nevertheless, this extensive array of configurations provides a multitude of degrees of freedom to accommodate diverse users, locations, and modulation rates within the network.

C. Codebook design

For a demonstration of MU multiplexing, we consider a broadcast node consisting of one single-frequency Tx and the metasurface, communicating to two Rxs (U_1 and U_2). We generate and experimentally evaluate a set of 1,000 metasurface configurations $\{V_i\}$. For each configuration, each of the 16 columns of the metasurface has a randomly applied bias V_i $(i=1,...,16)$ selected from a range of biases between 0 and -15 V with a step size of 0.25 V. Figures 6a and 6b show the resulting 1,000 constellation points measured at

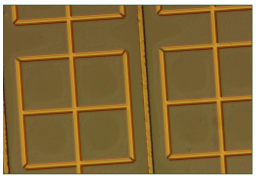

(a) S-SRR Pixel

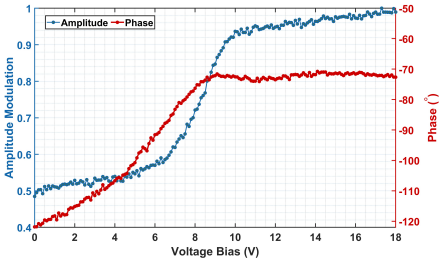

(b) Amplitude and phase modulation

Fig. 5: S-SRR meta-atom and corresponding phase shifts and amplitude modulation under uniform voltage biasing.

example angles $\theta_1 = 50°$ and $\theta_2 = 15°$ from the metasurface's broadside, respectively.

Here, the constellation point cloud for each user is normalized with respect to the user's maximum achieved amplitude value, since in communication systems, each user establishes their I-Q space using training symbols and based on the channel response between the user and the Tx [41]. We note that the constellations for both users encompass phase shift values spanning the entire 0 to 2π range. However, the achievable constellations are not distributed uniformly across the I-Q space. This is more prominent in this example for U_2 (shown in Fig. 6b). Such non-uniformity in constellation distribution can impact the availability of subsets of constellations needed to fulfill all symbol combinations. The uniform distribution allows the user to sustain higher modulation rates, given a certain BER constraint, compared to the less uniformly distributed constellation. Thus, users with non-uniform distributions might require higher SNR levels to achieve the same modulation rates compared to users with a more uniformly distributed constellations. We provide more discussion about this observation in Section V-D.

Next, we use these results to determine the best configuration subset corresponding to the modulation order for each user. Ideally, the resulting symbols for each user should be uniformly spaced over the I-Q space, resembling standard QAM constellations. However, precisely controlling all the features of the transmitted symbols with a realistic metasurface is extremely challenging. Alternatively, we select a subset of configurations (with a size of $2^{\sum_{i=1}^{N} M_i}$, where M_i is the modulation order of user i and N is the number of users) to collectively maximize the separation between symbols within each user's I-Q space. This process should yield sufficient separation between transmitted symbols to meet the targeted BER requirement for each user in the network. To do this, we first divide the constellation distribution for each user into 2^{M_i} sectors. Next, based on the modulation order of the next user, a joint problem is solved to find the $2^{(\sum_{i=1}^{N} M_i)}$ configurations (representing all symbols combinations) that yield constellations with the maximum separation distance for each user. We use a simple K-means algorithm to divide the set of each user to 2^{M_i} clusters [42]. Each cluster correspond to the points closest to each optimal point. finally, we find the best $2^{M_1+M_2}$ constellation points for each M_1 and M_2 combinations where $M_1 \in \{1, 2, 3, \dots\}$ and $M_2 \in \{1, 2, 3, \dots\}$, that yield constellations that jointly maximize the separation between the symbols in each user's I-Q space.

To illustrate this procedure with a worked example, we consider modulation orders for the two users as $M_1 = 2$ bits/symbol and $M_2 = 1$ bits/symbol, with the two users located at the same two angles mentioned above. We search through the 1,000 tested configurations to obtain the most separated points that satisfy the users' modulation orders. The blue and red constellation points in Fig. 6a and Fig. 6b illustrate the resulting subset of configurations for transmitting information symbols for U_1 and U_2, respectively. We see that these configurations, shown with red dots, provide $2^{M_1} = 4$ symbol options $\{00, 01, 10, 11\}$ for U_1 at θ_1, while the same configurations represent the same symbol $\{0\}$ for U_2 at θ_2. In addition, configurations shown with blue circles represent the symbol $\{1\}$ for U_2, while each configuration represents one of the available symbols for U_1. Therefore, the Tx can select one of these 8 configurations to simultaneously transmit two independent data streams to both users for all possible symbol combinations.

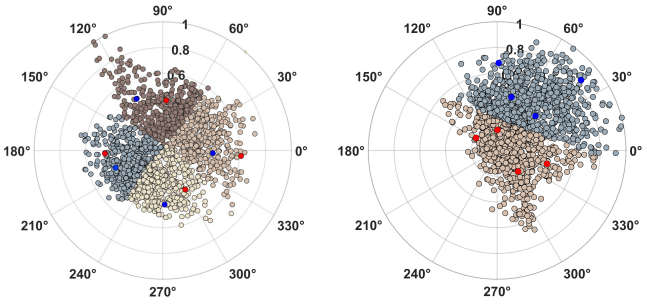

(a) Constellations Points at U_1 (b) Constellations Points at U_2

Fig. 6: The constellation points measured at U_1 and U_2, respectively, resulting from a set of 1000 random voltage configurations applied to the metasurface.

D. MU Gain

Given the non-uniform distribution of constellation points across different angles, as shown in Fig. 6, we show how our system can still concurrently transmit distinct symbols to two users positioned in different directions and shows significant gains against the SU case. Using the procedure outlined above, we evaluate our system 's MU performance

by utilizing the measured set of 1,000 constellations points to find the best $2^{M_1+M_2}$ constellation points for each M_1 and M_2 combinations for $M_1 \in \{1, 2, 3, \dots\}$ and $M_2 \in \{1, 2, 3, \dots\}$. Then, we numerically evaluate the selected constellation points to calculate the maximum achievable modulation rate.

As the THz time-domain platform we use for channel response measurements lacks the capability to transmit and receive modulated data, we resort to a Monte Carlo numerical simulation. Using measured results from our metasurface as inputs, this simulation finds the subsets required for each combination of modulation rates M_1 and M_2 to calculate the achievable aggregate MU rate and gains. Specifically, we use MATLAB to create two independent data streams, each with 10^5 pseudo-random symbols modulated at the Tx and received and demodulated at the considered Rx's directions. In the simulation, the required configuration from the measured subset is selected at every symbol time based on the set of symbols to be transmitted to the Rxs. Then, white Gaussian noise is added. Finally, upon receiving the entire stream, the BER at each Rx direction is calculated as the ratio of error bits to total bits. This ensures that our measurement-based simulation is based on the signal and metasurface response measured at the Rx. Finally, the maximum modulation rate achieved for each SNR is the maximum modulation rate achieved such that the BER for both users is less than 10^{-4}.

First, as a baseline, we compute the rates achieved when both users are served in a SU time-shared manner. In a time-shared system, when both users have sufficient SNR to be served, each user equally shares half of the available airtime. Therefore, the average SU rate at each SNR is computed as the average of the rates achieved by each user individually. Figure 7 shows the achieved rate for each user with the SU (time-shared) rate. First, we notice that there is a relatively moderate rate difference between the two locations. That is, due to the metasurface's angular response, in some instances one of the users can achieve the same rate at lower SNR relative to the other user. We can see that when both users have sufficient SNR to have a non-zero rate (SNR $>$ 10 dB), the SU rate is the average rate achieved by the two users. However, when one user is in outage (8 dB $\leq$ SNR $\leq$ 10 dB) the SU rate is the rate of the user being served. i.e., U_1. Finally, we notice that both users need SNR $>$ 7 dB to support a non-zero rate. As mentioned earlier, this is due to the fact the our metasurface has a relatively limited phase shift capabilities (around 50°) which result in some non-uniformity in the available constellation pool. We note that researchers have demonstrated switchable metasurfaces with larger ranges of phase control, which could offer even better performance in this low SNR regime [37].

Subsequently, we compare the rates achieved by our MU scheme with those achieved with the SU scheme. Figure 8a presents the aggregate MU rate ($M_1 + M_2$) along with the SU rates and Fig. 8b shows the achieved MU gain. There are three noticeable regimes, and we designate the central regime as the "Free-Rider Regime". In this mid-range SNR regime, our system manifests a maximum gain of twofold over the

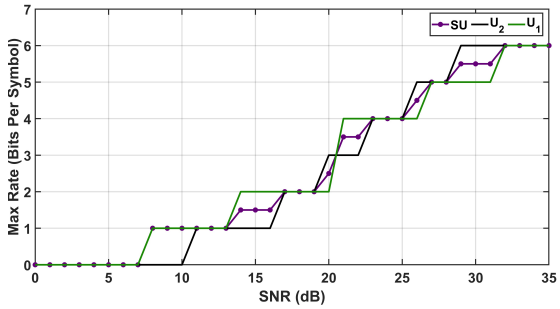

Fig. 7: The single user rates achieved at two angularly separated users.

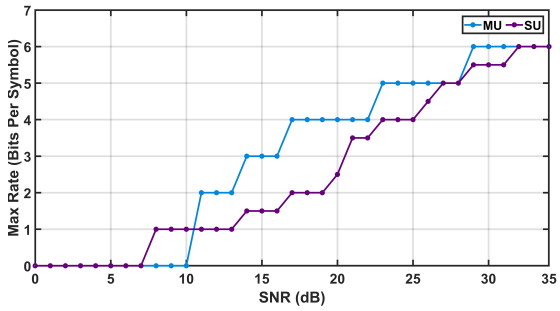

(a) **MU and SU Aggregate Rates**

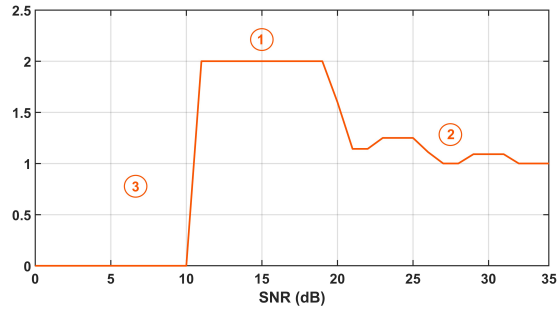

(b) **MU Gain**

Fig. 8: MU performance compared to SU.

SU scheme, as seen in Fig. 8b. That is, the network can accommodate a second "Free-Rider" Rx simultaneously without compromising the other user's rate if it was served alone (SU). Specifically, in addition to our system's capability to identify a set of constellations that fulfills the rate requirements for each user independently, it can leverage the available constellation pool to identify a supplementary symbol set to add a second user while conforming to the BER constraint of user one. Note that for a system accommodating n users, the maximum MU gain over SU is limited by the number of users n. That is, for the two-user scenario, a gain of twofold means that each user is utilizing all airtime at their respective maximum SU rates. In contrast, with higher SNR (labeled 2 in the figure), only moderate MU gains are achievable, surpassing unity but falling short of the maximum twofold gain. The reason for

this is that realizing the high SU rates while adding a new user necessitates an increased number of distinct constellation points, with new amplitude and phase values, to accommodate all possible symbol combinations.

As Fig. 5b shows, our programmable metasurface has a limited phase and amplitude response that constrains the diversity of constellation points achieved at certain angles. Consequently, sustaining U_1's rate at the maximum SU rate while introducing an additional user is not always possible. Instead, U_1's rate is reduced to accommodate U_2, while augmenting the sum rate. Thus, while our system may not attain the maximum potential MU gain, it still achieves significant gains in comparison to SU. Similarly, as can be seen in Fig 8b, as SNR increases, the MU gain diminishes until it reaches saturation at very high SNR values ($>$ 32 dB), wherein the performance of the MU and SU converges.

Finally, in the lower SNR range (labeled 3 in the figure), when one user experienced outage conditions (8 dB $\leq$ SNR $\leq$ 10 dB), the MU gain diminishes to below unity, rendering the SU scheme more favorable. This is because when U_2 is in outage, the network exclusively serves U_1, and it is allocated all available airtime, while U_2 is starved, resulting in better performance compared to our system that requires both users to have sufficient SNR to realize non-zero gains. Therefore, once U_2 emerges from outage, the network transitions into the previously delineated Free Rider range, where the MU scheme clearly outperforms the SU scheme.

We remark that our system yields gains even when both users share similar SNR values: This contrasts with previous Non-Orthogonal Multiple Access (NOMA) work, e.g., [19], [20], in which SNR diversity is essential for achieving MU gains.

MU Performance with Users SNR Diversity. As mentioned above, our system does not necessitate SNR diversity between users to achieve MU gains, however to further understand the MU performance, here we evaluate the potential MU achievable gains when the users experience different SNR values.

Here, we consider one user with a high SNR value of 35 dB (U_{High}), and a second user with varying SNR values (U_{Var}). We compare the MU performance with the SU performance and apply the same semi-analytical approach we adopted in the previous section to study the MU gains achieved in this case. Figure 9a shows the maximum achievable rate for the MU and SU cases. When U_{Var} is in outage the SU achieved rates are basically the rates achieved for U_{High} which have high SNR therefore the SU rates are high. On the other hand, the MU case cannot achieve nonzero rates when one user is in an outage. Thus, SU outperforms MU in this case. Once U_{Var} is out of outage and starts occupying half the air time, the MU rates rapidly increase to the maximum aggregate rate of 6 bits per symbol. On the other hand, the SU rates drop at first and then slowly increase as U_{Var} SNR increases. It can be seen from Fig. 9a that MU achieves the maximum rate at 15 dB SNR for U_{Var}, while SU requires both users to be in a high SNR condition, with U_{Var} being $\geq$ 27 dB. This signifies

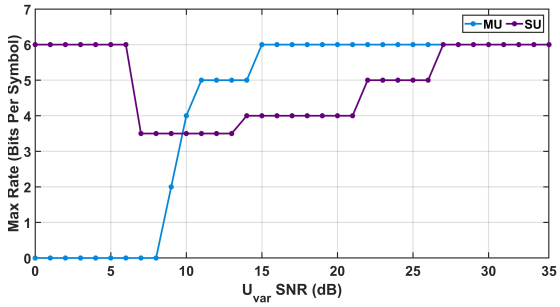

(a) **MU and SU Aggregate Rates**

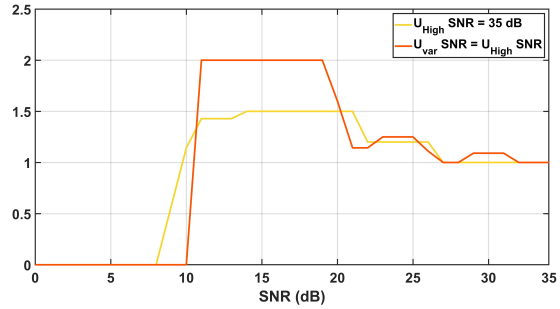

(b) **MU Gain**

Fig. 9: Comparison between MU and SU performance with users SNR differences.

the system's ability to achieve high aggregate rates, even when one user's SNR is not high enough to achieve these rates in the SU time shared scenario.

Figure 9b. shows the MU gains for this case compared to the gains achieved when the two users have equal SNR. While substantial MU gain of 1.5x is achieved, the system cannot achieve the maximum MU gain of 2. This limitation is attributed to the fact that one user, U_{High}, can support high SU rates and is in the saturation regime, constraining further gains, while user 2 is in the "free rider" regime, allowing a combined significant gain of 1.5x.

E. Angular Separation

Clearly, our approach relies on (and exploits) the angular separation among users to attain maximum MU gains. We explore this key feature by varying the angular separation $\Delta\theta$ between two users and computing the maximum aggregate rate at each position. Specifically, we maintain U_1 at a fixed angle $\theta_1 = 50^\circ$ while U_2 is positioned at different angular separations from U_1 with angular separation resolution of 1°. i.e., $\theta_2 = \{-50^\circ \text{ to } -20^\circ\}$, $\Delta\theta \in \{0^\circ \text{ to } 30^\circ\}$. The MU rate achieved at the two users' locations is utilized in conjunction with the SU rates to determine the achievable MU gain for each $\Delta\theta$.

Fig. 10 depicts the calculated MU gain for the specified $\Delta\theta$ set. Obviously, for $\Delta\theta = 0$, one expects no MU gain since the two users receive the same symbol. Indeed, our measurements show that, for an extremely small angular separation of 1°, the SU scheme outperforms the MU scheme, with MU gains

less than unity due to the similarity of received constellations from the same configurations at both users. However, as $\Delta\theta$ increases, the proposed approach achieves MU gains greater than 1 after only 2° of angular separation between U_1 and U_2. This shows that our approach can enable the transmission of independent data streams to users even if they are in close proximity. Thus, this idea enhances the overall network capacity compared to a single-user time-sharing scheme, even for users with small angular separation. As $\Delta\theta$ increases further, the achieved MU gain continues to increase until it reaches the maximum gain of twofold with only a 10° separation between the two users.

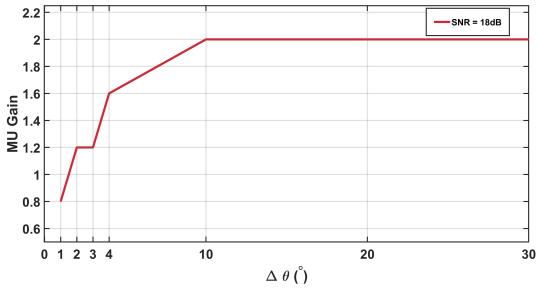

Fig. 10: The network's MU gains over the SU scheme achieved for different angular separations between U_1 and U_2.

To further study how the angular separation between users influences the similarity of constellations received at their respective directions, we evaluate the difference between the symbols received at the two users' locations from the same set of random configurations. To do so, we calculate the Average Symbol Distance (ASD), defined as the distance between the constellation points received at the two users' locations from the same configuration, averaged across the set of different configurations. This allows us to study how far apart the two users need to be in order to start receiving different symbols from the same configuration.

We compare the calculated ASD between the users' symbols, considering both the theoretical model outlined previously and the measurements discussed previously. The results, presented in Fig. 11, reveal that for the entire range of $\Delta\theta$, the distance between symbols received at the two users' locations increases until it reaches saturation near 10° separation. This suggests that the metasurface's response rapidly changes with increasing angular separation. However, we notice that the increase is nonmonotonic in both the model and the measurements. We also notice that there is high variance (shown in error bars and in the shaded area for both the measurements and the theoretical model, respectively) in the data. These fluctuations are inherent to utilizing random configurations, in which each configuration is independently generated from others. As a result, some configurations may lead to entirely different constellation points for the two users, while others may yield similar results, and our results are ultimately limited by statistical convergence. Nonetheless, the diverse and large number of achieved symbol sets allow us to select configurations that match the required requested symbols during actual data transmission. This demonstrates our system's capability of serving independent streams for users in congested and close proximity scenarios, with performance that is, in many cases, superior to the SU approach.

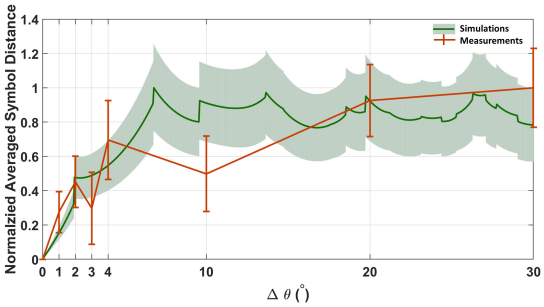

Fig. 11: Symbols distance between the constellations achieved from the same configuration at the two users' locations with different angular separation.

Lastly, there is an evident relationship between the symbol distance and achieved MU gains as a function of the angular separation between the users. Specifically, Fig. 11 shows that the average symbol distance between the two users is very low for an angular separation of 1°, corresponding to MU gains below unity for that $\Delta\theta$.

VI. Conclusion

We have reported a novel RF-chain-free sub-THz downlink MU access system based on a metasurface illuminated by a single, unmodulated sub-THz source. We show how a randomly generated metasurface configuration can result in distinct constellation points received at various user locations, allowing the transmission of simultaneous and independent symbols to users at different locations with a single configuration. Furthermore, we demonstrated that by generating a large number of such random metasurface configurations, we can achieve a wide range of symbol options for different users' locations and their corresponding modulation rate. We conducted over-the-air measurements to experimentally validate our proposed system using a transmissive metasurface with only 16 independent pixels. Even with this relatively small number of independent elements (and even though our metasurface has a limited range of phase modulation), we are still able to enable simultaneous independent transmissions to two users who are separated by only a few degrees. Our measurements show that within a certain range of SNR values at the Rxs, we achieve the maximum MU gains of twofold, in comparison with a conventional single-user scenario. In addition, we show that the MU gain can exceed conventional single-user methods under a wide range of operating conditions under very small angular separation between the Rxs. In future work, we aim to address challenges associated with scaling to larger user populations. This includes developing strategies for user selection to maximize different utility functions such as network total throughput and fairness between users.

REFERENCES

[1] A. Shafie, N. Yang, C. Han, J. M. Jornet, M. Juntti, and T. Kürner, "Terahertz communications for 6g and beyond wireless networks: Challenges, key advancements, and opportunities," *IEEE Network*, vol. 37, no. 3, pp. 162–169, 2023.

[2] M. Polese, X. Cantos-Roman, A. Singh, M. J. Marcus, T. J. Maccarone, T. Melodia, and J. M. Jornet, "Coexistence and spectrum sharing above 100 GHz," *Proceedings of the IEEE*, vol. 111, no. 8, pp. 928–954, 2023.

[3] A. Singh, V. Petrov, H. Guerboukha, I. V. Reddy, E. W. Knightly, D. M. Mittleman, and J. M. Jornet, "Wavefront engineering: Realizing efficient terahertz band communications in 6g and beyond," *IEEE Wireless Communications*, vol. 31, no. 3, pp. 133–139, 2024.

[4] Y. Ghasempour, C. R. C. M. da Silva, C. Cordeiro, and E. W. Knightly, "IEEE 802.11ay: Next-generation 60 GHz communication for 100 gb/s Wi-Fi," *IEEE Communications Magazine*, vol. 55, no. 12, pp. 186–192, 2017.

[5] C. Chen, X. Chen, D. Das, D. Akhmetov, and C. Cordeiro, "Overview and performance evaluation of Wi-Fi 7," *IEEE Communications Standards Magazine*, vol. 6, no. 2, pp. 12–18, 2022.

[6] Y. Ghasempour, M. K. Haider, C. Cordeiro, and E. W. Knightly, "Multi-user multi-stream mmwave wlans with efficient path discovery and beam steering," *IEEE Journal on Selected Areas in Communications*, vol. 37, no. 12, pp. 2744–2758, 2019.

[7] A. Alkhateeb, G. Leus, and R. W. Heath, "Limited feedback hybrid precoding for multi-user millimeter wave systems," *IEEE Transactions on Wireless Communications*, vol. 14, no. 11, pp. 6481–6494, 2015.

[8] M.-S. Kim, T. Ropitault, S. Lee, N. Golmie, H. Assasa, and J. Widmer, "A link quality estimation-based beamforming training protocol for IEEE 802.11ay MU-MIMO communications," *IEEE Transactions on Communications*, vol. 69, no. 1, pp. 634–648, 2021.

[9] P. Sen, J. V. Siles, N. Thawdar, and J. Jornet, "Multi-kilometre and multi-gigabit-per-second sub-terahertz communications for wireless backhaul applications," *Nature Electron.*, vol. 6, pp. 164–175, 2022.

[10] J. Jornet, E. Knightly, and D. Mittleman, "Wireless communications sensing and security above 100 GHz," *Nature Commun.*, vol. 14, p. 841, 2023.

[11] T. Kürner, D. M. Mittleman, and T. Nagatsuma, "Introduction to THz Communications," in *THz Communications: Paving the Way Towards Wireless Tbps*, Springer, 2022.

[12] X. Yang, M. Matthaiou, J. Yang, C.-K. Wen, F. Gao, and S. Jin, "Hardware-constrained millimeter-wave systems for 5G: Challenges, opportunities, and solutions," *IEEE Communications Magazine*, vol. 57, no. 1, pp. 44–50, 2019.

[13] C. Han, L. Yan, and J. Yuan, "Hybrid beamforming for terahertz wireless communications: Challenges, architectures, and open problems," *IEEE Wireless Communications*, vol. 28, no. 4, pp. 198–204, 2021.

[14] D. M. Bodet and J. M. Jornet, "Directional antennas for sub-thz and THz MIMO systems: Bridging the gap between theory and implementation," *IEEE Open Journal of the Communications Society*, vol. 4, pp. 2261–2273, 2023.

[15] S. Faghih-Naini, C. Sebastian, T. Reissland, R. Weigel, and B. Scheiner, "Hardware design challenges and modulation schemes in joint communication and sensing: Analyzation and comparison of the state-of-the-art co-located communication and sensing systems," *IEEE Microwave Magazine*, vol. 25, no. 3, pp. 84–97, 2024.

[16] S. Abu-Surra, W. Choi, S. Choi, E. Seok, D. Kim, N. Sharma, S. Advani, V. Loseu, K. Bae, I. Na, A. A. Farid, M. J. W. Rodwell, G. Xu, and J. C. Zhang, "End-to-end 140 GHz wireless link demonstration with fully-digital beamformed system," in *2021 IEEE International Conference on Communications Workshops (ICC Workshops)*, pp. 1–6, 2021.

[17] C. Lin and G. Y. L. Li, "Terahertz communications: An array-of-subarrays solution," *IEEE Communications Magazine*, vol. 54, no. 12, pp. 124–131, 2016.

[18] D. Bodet, P. Sen, Z. Hossain, N. Thawdar, and J. M. Jornet, "Hierarchical bandwidth modulations for ultra-broadband communications in the terahertz band," *IEEE Transactions on Wireless Communications*, vol. 22, no. 3, pp. 1931–1947, 2023.

[19] K. P. Dasala, J. M. Jornet, and E. W. Knightly, "Scaling mmwave wlans with single rf chain multiuser beamforming," *IEEE/ACM Transactions on Networking*, vol. 30, no. 6, pp. 2630–2643, 2022.

[20] Z. Wei, L. Zhao, J. Guo, D. W. K. Ng, and J. Yuan, "A multi-beam noma framework for hybrid mmWave systems," in *2018 IEEE International Conference on Communications (ICC)*, pp. 1–7, 2018.

[21] H. Zhang, Y. Duan, K. Long, and V. C. M. Leung, "Energy efficient resource allocation in terahertz downlink NOMA systems," *IEEE Transactions on Communications*, vol. 69, no. 2, pp. 1375–1384, 2021.

[22] B. Ning, Z. Chen, W. Chen, Y. Du, and J. Fang, "Terahertz multi-user massive MIMO with intelligent reflecting surface: Beam training and hybrid beamforming," *IEEE Transactions on Vehicular Technology*, vol. 70, no. 2, pp. 1376–1393, 2021.

[23] M. Rahim, T. L. Nguyen, G. Kaddoum, and T. N. Do, "Multi-irs-aided terahertz networks: Channel modeling and user association with imperfect csi," *IEEE Open Journal of the Communications Society*, vol. 5, pp. 836–855, 2024.

[24] B. Ning, P. Wang, L. Li, Z. Chen, and J. Fang, "Multi-IRS-aided multi-user MIMO in mmwave/thz communications: A space-orthogonal scheme," *IEEE Transactions on Communications*, vol. 70, no. 12, pp. 8138–8152, 2022.

[25] R. Chen, M. Chen, X. Xiao, W. Zhang, and J. Li, "Multi-user orbital angular momentum based terahertz communications," *IEEE Transactions on Wireless Communications*, vol. 22, no. 9, pp. 6283–6297, 2023.

[26] C. Lin and G. Y. L. Li, "Terahertz communications: An array-of-subarrays solution," *IEEE Communications Magazine*, vol. 54, no. 12, pp. 124–131, 2016.

[27] S. A. Busari, K. M. S. Huq, S. Mumtaz, and J. Rodriguez, "Terahertz massive MIMO for beyond-5G wireless communication," in *ICC 2019 - 2019 IEEE International Conference on Communications (ICC)*, pp. 1–6, 2019.

[28] Z. Chen, X. Ma, B. Zhang, Y. Zhang, Z. Niu, N. Kuang, W. Chen, L. Li, and S. Li, "A survey on terahertz communications," *China Communications*, vol. 16, no. 2, pp. 1–35, 2019.

[29] K. P. Dasala and E. W. Knightly, "Multi-user terahertz WLANs with angularly dispersive links," in *Proceedings of the Twenty-Third International Symposium on Theory, Algorithmic Foundations, and Protocol Design for Mobile Networks and Mobile Computing*, MobiHoc '22, (New York, NY, USA), p. 121–130, Association for Computing Machinery, 2022.

[30] M. P. Daly, E. L. Daly, and J. T. Bernhard, "Demonstration of directional modulation using a phased array," *IEEE Trans. Antennas Propag.*, vol. 58, pp. 1545–1550, 2010.

[31] W. Tang, M. Z. Chen, J. Y. Dai, Y. Zeng, X. Zhao, S. Jin, Q. Cheng, and T. J. Cui, "Wireless communications with programmable metasurface: New paradigms, opportunities, and challenges on transceiver design," *IEEE Wireless Commun.*, vol. 27, pp. 180–187, 2020.

[32] L. Zhang, M. Chen, W. Tang, J. Y. Dai, L. Miao, X. Zhou, S. Jin, Q. Cheng, and T. J. Cui, "A wireless communication scheme based on space- and frequency-division multiplexing using digital metasurfaces," *Nature Electron.*, vol. 4, pp. 218–227, 2021.

[33] X. Wan, Q. Zhang, T. Chen, L. Zhang, W. Xu, H. Huang, C. Xiao, Q. Xiao, and T. J. Cui, "Multichannel direct transmissions of near-field information," *Light: Sci. Appl.*, vol. 8, p. 60, 2019.

[34] J. W. Goodman, "Introduction to fourier optics, roberts & co," *Publishers, Englewood, Colorado*, 2005.

[35] M. Koch, D. Mittleman, J. Ornik, and E. Castro-Camus, "Terahertz time-domain spectroscopy," *Nature Rev. Methods Primers*, vol. 3, p. 48, 2023.

[36] S. Venkatesh, X. lu, H. Saeidi, and K. Sengupta, "A high-speed programmable and scalable terahertz holographic metasurface based on tiled CMOS chips," *Nature Electronics*, vol. 3, pp. 1–9, 12 2020.

[37] F. Lan, L. Wang, H. Zeng, S. Liang, T. Song, W. Liu, P. Mazumder, Z. Yang, Y. Zhang, and D. M. Mittleman, "Real-time programmable metasurface for terahertz multifunctional wave front engineering," *Light Sci. Appl.*, vol. 12, p. 191, 2023.

[38] N. M. Monroe, G. C. Dogiamis, R. Stingel, P. Myers, X. Chen, and R. Han, "Electronic thz pencil beam forming and 2D steering for high angular-resolution operation: A 98 $\times$ 98-unit 265GHz CMOS reflectarray with in-unit digital beam shaping and squint correction," in *2022 IEEE International Solid-State Circuits Conference (ISSCC)*, pp. 1–3, 2022.

[39] H.-T. Chen, W. Padilla, O. Joshua, A. Gossard, A. Taylor, and R. Averitt, "Active terahertz metamaterial devices," *Nature*, vol. 444, pp. 597–600, 12 2006.

[40] W. Padilla, M. Cich, A. Azad, R. Averitt, A. Taylor, and H.-T. Chen, "A metamaterial solid-state terahertz phase modulator," *Nature Photon.*, vol. 3, pp. 148–151, 2009.

[41] J. G. Proakis, *Digital Communications*. McGraw-Hill, 1995.

[42] S. Lloyd, "Least squares quantization in pcm," *IEEE Transactions on Information Theory*, vol. 28, no. 2, pp. 129–137, 1982.